



JGR Biogeosciences

RESEARCH ARTICLE

10.1029/2023JG007381

Special Section:

The Earth in living color: spectroscopic and thermal imaging of the Earth: NASA's Decadal Survey Surface Biology and Geology Designated Observable

Key Points:

- We compared three soil moisture retrieval models, multilayer radiative transfer model of soil reflectance (MARMIT), soil water parametric (SWAP)-Hapke, and a variant, using hyperspectral UAS imagery and goniometer data
- Best models were: modified (SWAP)-Hapke model (directional source/goniometer); MARMIT (UAS imagery/direct solar and diffuse skylight)
- Differences in model treatment of the equivalent water layer likely contribute to these different outcomes depending on illumination

Correspondence to:

N. B. Nur and C. M. Bachmann, nn6721@rit.edu; Charles.Bachmann@rit.edu

Citation:

Nur, N. B., & Bachmann, C. M. (2023). Comparison of soil moisture content retrieval models utilizing hyperspectral goniometer data and hyperspectral imagery from an unmanned aerial system. *Journal of Geophysical Research: Biogeosciences*, 128, e2023JG007381. https://doi.org/10.1029/2023JG007381

Received 16 JAN 2023 Accepted 21 MAY 2023 Corrected 3 JUL 2023

This article was corrected on 3 JUL 2023. See the end of the full text for details.

© 2023. The Authors.

This is an open access article under the terms of the Creative Commons Attribution License, which permits use, distribution and reproduction in any medium, provided the original work is properly cited.

Comparison of Soil Moisture Content Retrieval Models Utilizing Hyperspectral Goniometer Data and Hyperspectral Imagery From an Unmanned Aerial System

Nayma Binte Nur¹ o and Charles M. Bachmann¹

¹Chester F. Carlson Center for Imaging Science, Rochester Institute of Technology, Rochester, NY, USA

Abstract To understand surface biogeophysical processes, accurately evaluating the geographical and temporal fluctuations of soil moisture is crucial. It is well known that the surface soil moisture content (SMC) affects soil reflectance at all solar spectrum wavelengths. Therefore, future satellite missions, such as the NASA Surface Biology and Geology mission, will be essential for mapping and monitoring global soil moisture changes. Our study compares two widely used moisture retrieval models: the multilayer radiative transfer model of soil reflectance (MARMIT) and the soil water parametric (SWAP)-Hapke model. We evaluated the SMC retrieval accuracy of these models using unmanned aerial systems (UAS) hyperspectral imagery and goniometer hyperspectral data. Laboratory analysis employed hyperspectral goniometer data of sediment samples from four locations reflecting diverse environments, while field validation used hyperspectral UAS imaging and coordinated ground truth collected in 2018 and 2019 from a barrier island beach at the Virginia Coast Reserve Long-Term Ecological Research site. The (SWAP)-Hapke model achieves comparable accuracy to MARMIT using laboratory hyperspectral data but is less accurate when applied to UAS hyperspectral imagery than the MARMIT model. We proposed a modified version of the (SWAP)-Hapke model, which achieves better results than MARMIT when applied to laboratory spectral measurements; however, MARMIT's performance is still more accurate when applied to UAS imagery. These results are likely due to differences in the models' descriptions of multiply-scattered light and MARMIT's more detailed description of air-water interactions.

Plain Language Summary Understanding how soil moisture content (SMC) changes is crucial because it plays a significant role in many environmental processes. This study compares three models using hyperspectral data and imagery from the laboratory and a barrier island field setting to find the most effective method for mapping SMC over large areas with the larger goal of application to global scales using the future NASA Surface Biology and Geology mission hyperspectral imagery. We considered three physics-based models: the multilayer radiative transfer model of soil reflectance (MARMIT) model, the SWAP-Hapke model, and a modified version of the SWAP-Hapke model. To better model retrieval of SMC in the landscape from imagery, we used a hyperspectral imaging system, which has a higher information capacity than traditional RGB and multispectral imagery, to collect imagery over field validation sites from an unmanned aerial system (UAS), while the laboratory hyperspectral data was collected from samples, acquired in four different locations, using a hyperspectral goniometer. Differences in underlying model assumptions favor the modified (SWAP)-Hapke model for laboratory data where illumination is solely from a directional source, while the MARMIT performs best with the field UAS imagery where both the direct solar and diffuse skylight illuminate the soil.

1. Introduction

Soil moisture content (SMC) is a prominent geophysical variable that is a vital factor in many processes, including carbon cycle, energy budget, erosion, evapo-transpiration, global annual photosynthesis, infiltration, and rainfall-runoff (Berg & Sheffield, 2018; Green et al., 2019; Jaeger & Seneviratne, 2011; Kirkby, 2016; Ochsner et al., 2013; Shepherd et al., 2002; Stocker et al., 2019), making accurate retrieval of this geophysical parameter an essential objective in agriculture, civil engineering, hydrology, micrometeorology, military applications, and other environmental disciplines (Gardner et al., 2000; Ochsner et al., 2013; Robinson et al., 2008; Vereecken et al., 2008; Wang & Qu, 2009). For agriculture, hydrology, planetary research, and military applications, remote sensing has been utilized to estimate SMC readings in the solar (350–2,500 nm), thermal infrared (3–12 µm), and microwave (0.5–100 cm) domains since the 1970s (Babaeian et al., 2019; Dong et al., 2020; Li et al., 2022; Mulder et al., 2011;

NUR AND BACHMANN 1 of 21

Mohanty et al., 2017; Ochsner et al., 2013; Petropoulos et al., 2018; X. Yang et al., 2019). However, field measurements are not optimal for large-scale mapping since SMC varies significantly in time and space (Gardner et al., 2000). Due to its greater information capacity, hyperspectral imaging has a distinct advantage over typical RGB and multispectral imagery for near-surface geophysical mapping of surface conditions, including SMC. Imaging systems on both satellites and unmanned aerial systems (UAS) enable more economical SMC mapping. UAS have numerous uses, including in agriculture (Ezenne et al., 2019; Hunt et al., 2014; Shafian et al., 2018), industry (Padró et al., 2019; Rakha & Gorodetsky, 2018; Shukla & Karki, 2016), environmental science (Palace et al., 2018), and the military (Chahl, 2015), however, satellite systems provide global access, not possible with UAS imagery, to critical variables such as SMC. The future NASA Surface Biology and Geology Mission (SBG), because of the planned high signal-to-noise ratio (SNR) and fine-spectral resolution reflectance imagery with 30m ground sample distance (GSD) spatial resolution, proposed in the Science and Applications Traceability Matrix (SATM) (NASA Surface Biology and Geology Mission Science and Applications Traceability Matrix, Accessed: 09 May 2023), will provide global access to SMC and other critical geophysical variables at a much higher level of accuracy and spatial detail than has been possible with preceding multi-spectral satellite systems.

In this work, we compare the MARMIT model (Bablet et al., 2018, 2020) and (SWAP)-Hapke model (G.-J. Yang et al., 2011) as well as a modified version of the (SWAP)-Hapke model. In the MARMIT model (Bablet et al., 2018, 2020), the embedded SMC is treated as a layer of equivalent water thickness with an assumed efficiency value that models the fraction of wet surface area present at a specific location. The model divides the soil and embedded water into separate but equivalent layers and employs the well-known Fresnel formalism to reflect and transmit light at their respective boundaries. This model uses Fresnel coefficients to characterize subsequent orders of internal reflection and transmission factors at the soil-to-water and air-to-water interfaces and the Beer-Lambert equation to simulate absorption during each transit between borders. G.-J. Yang et al. (2011), however, utilized Hapke's radiative transfer model solution (Hapke, 1981) to determine soil moisture content. The Hapke model solution separates the surface soil radiance of the sensor into single and multiple scattering, with the latter assumed to be isotropic, however, in Yang's (SWAP)-Hapke model, water content is modeled only by a Beer-Lambert extinction factor, that multiplies the Hapke solution to the radiative transfer equation, in an equivalent water layer (G.-J. Yang et al., 2011).

This study compares MARMIT, the (SWAP)-Hapke model, and a modified version of the (SWAP)-Hapke model using both laboratory hyperspectral goniometer data and field hyperspectral imagery. We utilized four distinct types of samples from four locations in the laboratory study, which employed hyperspectral goniometer data. For the field analysis, we used hyperspectral unmanned aerial system (UAS) imagery from various geometries and times of day to validate the models described and accompanying ground truth data collected as part of large field campaigns at the Virginia Coast Reserve Long-Term Ecological Research (VCR-LTER) (Virginia Coast Reserve Long Term Ecological Research site, Accessed: 09 May 2023) site in July 2018 and July 2019.

2. Materials and Methods

2.1. Theory

2.1.1. MARMIT Model

MARMIT depicts wet soil as dry soil coated with a separate layer of water (Bablet et al., 2018). This layer is an equivalent water layer, representing the effect of water embedded within the soil. MARMIT is a member of a class of radiative transfer models known as equivalent slab models (Hapke, 2012) and builds on earlier models developed by Ångström (1925), Lekner and Dorf (1988), Bach and Mauser (1994), and others.

In the MARMIT model, the reflectance of wet soil is modeled as a weighted sum of dry and wet soil reflectance:

$$R_{\text{MARMIT}} = \varepsilon R_{ws} + (1 - \varepsilon) R_d \tag{1}$$

Here, ε varies between 0 and 1, R_d is the reflectance of fully dry soil, and R_{ws} is the reflectance of completely wet soil. The weighted sum allows the description of a range of conditions, from fully dry soil to partially or fully wet soil. To simplify the equations, the wavelength dependence of the reflectances is not shown in Equation 1.

MARMIT assumes that R_d can be measured, and R_{ws} can be calculated using the following expression, which results from the addition of an infinite series of orders of multiple-scattered light interacting with each boundary (air-water and water-soil):

NUR AND BACHMANN 2 of 21

$$R_{ws} = r_{12} + \frac{t_{12}t_{21}R_dT_w^2}{1 - r_{21}R_dT_w^2} \tag{2}$$

Here, the reflectance and transmission of light arriving at the equivalent water layer from the air, r_{12} and t_{12} , are related according to:

$$r_{12} = 1 - t_{12} \tag{3}$$

where both r_{12} and t_{12} are calculated from the Fresnel equations for unpolarized collimated light. Thus, r_{12} and t_{12} depend only on the indices of refraction of air and water and the angle of incidence of the light.

However, internal reflection and transmission at the air-water interface, r_{21} and t_{21} are treated differently. MARMIT assumes a diffuse form obtained by averaging the Fresnel equation over the hemisphere, using results of the earlier work of Lekner and Dorf (1988) and Stern (1961). As a result, r_{21} depends only on the refractive indices of the media (water and air).

$$r_{21} = 1 - \frac{1}{n^2} \left(1 - r'_{12} \right) \tag{4}$$

where,

$$r'_{12} = \frac{3n^2 + 2n + 1}{3(n+1)^2} - \frac{2n^3(n^2 + 2n - 1)}{(n^2 + 1)^2(n^2 - 1)} + \frac{n^2(n^2 + 1)}{(n^2 - 1)^2} \log n - \frac{n^2(n^2 - 1)^2}{(n^2 + 1)^2} \log \frac{n(n+1)}{n-1}$$
(5)

and assuming that the index of refraction of air $n_a \equiv 1$, this reduces to dependence solely on the index of refraction of water. Furthermore, t_{21} also only depends on the relative refractive index of water since:

$$t_{21} = 1 - r_{21} \tag{6}$$

Finally, T_w is the transmittance of the water layer, which in MARMIT uses the Beer-Lambert-Bouguer law:

$$T_w = e^{-\alpha_B L} \tag{7}$$

where α_B is the water absorption coefficient (Palmer & Williams, 1974).

After optimization of L and ϵ in the first stage of the MARMIT model, in the second stage, the optimized L and ϵ values are fit through an assumed logistic calibration function to the measured SMC:

$$SMC = \frac{A}{1 + Be^{-\psi\Phi}} \tag{8}$$

where A is the logistic function's highest (asymptotic) value, ψ is the curve's steepness, and Φ denotes the mean equivalent water thickness, expressed by:

$$\Phi = L \times \varepsilon \tag{9}$$

2.1.2. (SWAP)-Hapke Model

In the (SWAP)-Hapke model, to retrieve the moisture content of the soil, G.-J. Yang et al. (2011) used the SOILSPECT (Jacquemoud et al., 1992) model, an improved version of the Hapke model (Hapke, 1981), including, in addition, an equivalent water layer to model embedded soil moisture. The approximate solution to the radiative transfer equation proposed by Hapke is a frequently used bi-directional reflectance model for soils (Shepard & Helfenstein, 2011; Domingue & Hapke, 1989; Domingue & Verbiscer, 1997; Hartman & Domingue, 1998; Verhoef & Bach, 2007; Shepard & Helfenstein, 2007; Wu et al., 2009; G.-J. Yang et al., 2011; Ciarniello et al., 2011; Helfenstein & Shepard, 2011; Shepard & Helfenstein, 2011; Schmidt & Fernando, 2015) that treats single scattering exactly but approximates multiple scattering as isotropic. This isotropic multiple scattering approximation (IMSA) model is based on the Chandrasekhar–Ambartsumian Method of Invariance (Ambartsumian, 1944; Chandrasekhar, 1960; Hapke, 1981, 2012). The sum of exact single scattering, r_{ss} , and approximate multiple scattering, r_{m} , yields an approximate solution to the radiative

NUR AND BACHMANN 3 of 21

transfer equation. The exact single scattering contribution incorporates the single scattering phase function; however, the phase function for multiple scattering contributions is considered to be isotropic ($p_{multiple\ scattering} = 1$).

Yang's bidirectional reflectance model of soil uses the form of the reflectance in Hapke's IMSA model, but omits the porosity function that Hapke included in later versions of his model (Hapke, 2012). Here we show the form appropriate to the bidirectional reflectance factor (BRF), rather than bidirectional reflectance (Hapke's original form) or bi-directional reflectance distribution factor (BRDF), since BRF is appropriate to the data measured in our laboratory and field settings which were in reference to a reflectance standard material or set of materials. In some analyses, BRF is referred to as a theoretical construct while data collected in the laboratory setting is described as bi-conical reflectance factor (BCRF) (Nicodemus et al., 1977) in reference to the small but finite nature of the apertures of source and sensor in this context. In the UAS-based hyperspectral imagery described later, the terminology sometimes used is hemispherical conical reflectance factor (HCRF) (Schaepman-Strub et al., 2006), to indicate that light originates from anywhere in the hemisphere (in this study, the directional solar illumination and diffuse skylight), while the sensor aperture remains small and finite. For a directional source, Hapke's solution (BRF description) to the radiative transfer equation with exact single scattering and isotropic multiple scattering has the form (Hapke, 2012):

$$r(\theta_{i}, \theta_{e}, g) = r_{s}(\theta_{i}, \theta_{e}, g) + r_{m}(\theta_{i}, \theta_{e}, g)$$

$$= \frac{w(\lambda)}{4} \frac{1}{\mu_{i} + \mu_{e}} (\{p(g, g', \lambda)[1 + B(g, \lambda)]\} + \{H[\mu_{i}, w(\lambda)]H[\mu_{e}, w(\lambda)] - 1\})$$
(10)

where, μ_i and μ_e are the direction cosines for the incident zenith angle, θ_i , and the scattered zenith angle, θ_e , respectively; $w(\lambda)$ is the single scattering albedo; $H[\mu_i, w(\lambda)]$ and $H[\mu_e, w(\lambda)]$ are respectively incident and view-angle Chandrasekhar–Ambartsumian H functions, and $p(g, g', \lambda)$ is the single particle scattering phase function. G.-J. Yang et al. (2011) used an approximate form of the *H*-function, originally used by Hapke, that is accurate to within 4% (Hapke, 1981):

$$H(\mu) = \frac{1 + 2\mu}{1 + 2\mu\sqrt{1 - w}} \tag{11}$$

In (SWAP)-Hapke, G.-J. Yang et al. (2011) uses the modified phase function described in SOILSPECT (Jacquemoud et al., 1992), which depends on both the phase angle g as well as g', the angle between the specular reflection direction and the incident light direction:

$$P(g, g', \lambda) = 1 + b\cos(g) + \frac{c(3\cos^2(g) - 1)}{2} + b'\cos(g') + \frac{c'(3\cos^2(g') - 1)}{2}$$
(12)

where, b, c, b' and c' are coefficients of the scattering phase function, and the angles g and g' satisfy:

$$\cos(g) = \cos(\theta_i)\cos(\theta_e) + \sin(\theta_i)\sin(\theta_e)\cos(\phi) \tag{13}$$

$$\cos(g') = \cos(\theta_i)\cos(\theta_e) - \sin(\theta_i)\sin(\theta_e)\cos(\phi) \tag{14}$$

where ϕ is the relative azimuth between the sun and the observation direction. In Equation 10, B(g) describes the shadow-hiding opposition effect (SHOE) (Hapke, 1986, 2012):

$$B(g) = \frac{B_{S0}}{1 + \frac{1}{h} \tan\left(\frac{g}{2}\right)} \tag{15}$$

Here, h represents the half-width parameter of the opposition effect (also known as the hot spot), which depends on properties of the medium including fill factor and grain size distribution (Hapke, 2012), whereas B_{S0} defines its scale.

In (SWAP)-Hapke, G.-J. Yang et al. (2011) used the SOILSPECT model first to estimate the reflectance of the dry soil and, later, introduced an equivalent water thickness, *L*, to estimate the reflectance of wet soil using the Beer-Lambert law:

$$R_{ws} = R_{ds}e^{-\alpha L} \tag{16}$$

NUR AND BACHMANN 4 of 21

doi/10.1029/2023JG007381 by UNIVERSITY OF VIRGINIA, Wiley Online Library on [14/11/2023]. See

where, α represents the extinction coefficient of water (cm⁻¹), L is the equivalent water thickness of soil moisture (cm), R_{ds} is the estimated dry soil reflectance from the SOILSPECT model, and R_{ws} is the double-hemisphere reflectance of wet soil.

2.1.3. Modified (SWAP)-Hapke Model

In our modified version of (SWAP)-Hapke model, we added the porosity factor, $K(\phi)$, originally defined by Hapke to describe the dependence of extinction on the filling factor ϕ of the medium. $K(\phi)$ has the form (Hapke, 2008, 2012):

$$K(\phi) \approx -\frac{\ln(1 - 1.209\phi^{2/3})}{1.209\phi^{2/3}}$$
 (17)

The original (SWAP)-Hapke model ignored the effect of the filling factor described in the porosity factor. Likewise, we also replaced the 4%-error H function with the improved 1%-error H-function developed by Hapke in later versions of his Isotropic Multiple Scattering Approximation (IMSA) model (Hapke, 2002, 2012). Thus, we used the reflectance defined in the more modern version of IMSA by:

$$r(\theta_i, \theta_e, g) = K(\phi) \frac{w(\lambda)}{4} \frac{1}{\mu_i + \mu_e} (p(g, \lambda)(1 + B_S(g, K(\phi), \lambda))$$
(18)

$$+\left(H\left[\frac{\mu_i}{K(\phi)}, w(\lambda)\right] H\left[\frac{\mu_e}{K(\phi)}, w(\lambda)\right] - 1\right)$$
 (19)

with the H-function given by:

$$H\left[\frac{\mu}{K(\phi)}, w(\lambda)\right] = \frac{1}{1 - w(\lambda) \frac{\mu}{K(\phi)} \left[r_0 + \frac{1 - 2r_0 \frac{\mu}{K(\phi)}}{2} \ln\left(\frac{1 + \frac{\mu}{K(\phi)}}{\frac{\mu}{K(\phi)}}\right)\right]}$$
(20)

Here, r_0 is the diffusive reflectance derived by Hapke using a two-stream radiative transfer model (Hapke, 2012):

$$r_0 = \frac{1 - \gamma}{1 + \gamma} = \frac{1 - \sqrt{1 - w(\lambda)}}{1 + \sqrt{1 - w(\lambda)}}$$
 (21)

and $\gamma = 1 - \sqrt{1 - w(\lambda)}$ is the albedo factor. As before, $B_S(g, K(\phi), \lambda)$ describes the correction to the single-scattering component representing the shadow hiding opposition effect (SHOE), a brightening noticed at smaller phase angles, usually lower than 20°. We again used Hapke's approximate form for the SHOE, which has the form found in Equation 15. In that equation, B_{S0} is a free constant that is optimized during the inversion process. However, the width of the SHOE peak, h, implemented by us here uses a form defined in (Bachmann, Eon, Ambeau, et al., 2018):

$$h = \beta K(\phi)\phi \tag{22}$$

where, as before, ϕ is the filling factor of the sediment, and β is a free parameter to be optimized during the inversion process. The free parameter β here was originally suggested as a pre-factor to reflect the fact that the overall constant multiplying $K(\phi)\phi$ typically depends on the grain size distribution(Hapke, 2012), which is expected to vary in the landscape (Bachmann, Eon, Ambeau, et al., 2018).

Instead of the SOILSPECT phase function, in our modified (SWAP)-Hapke model, we choose a Legendre polynomial series phase function:

$$p(g) = \sum_{l=0}^{N} a_l P_l(\cos(g))$$
 (23)

In the models described here, we chose N = 4:

$$p(g) = a_0 + a_1 \cos(g) + a_2 \left[\frac{1}{2} (3\cos^2(g)) - 1 \right] + a_3 \left[\frac{1}{2} (5\cos^3(g)) - 3\cos(g) \right]$$

$$+ a_4 \left[\frac{1}{8} (35\cos^4(g)) - 30\cos^2(g) + 3 \right]$$
(24)

NUR AND BACHMANN 5 of 21

Here, $a_0 = 1$ and the free parameters $a_1, ..., a_4$ are all optimized during the inversion process. Lastly, we included an efficiency parameter similar to the MARMIT model (Bablet et al., 2018) (Equation 1) to reflect the proportion of wet soil present in the soil matrix.

2.2. Comparison Strategy

In order to compare the models, the SMC was calculated identically for each model. We used the MARMIT model's assumed logistic function (Bablet et al., 2018) to describe the relationship between SMC and mean equivalent water layer thickness in each case.

In order to assess each model's performance, we determined the normalized root mean square error (*NRMSE*). The *NRMSE*, also referred to as the "Scatter Index" (Bonakdar et al., 2016; Kisi et al., 2013), is the ratio of the mean squared error to the mean measured value (Bonakdar et al., 2016; Zhao et al., 2020):

$$NRMSE = \frac{\sqrt{\frac{1}{N} \sum_{j=1}^{N} (SMC_{j,pred} - SMC_{j,meas})^2}}{\overline{SMC_{meas}}}$$
(25)

Here, SMC_{jpred} and SMC_{jmeas} denote the predicted SMC value and the measured SMC value, respectively, for the jth sample in the specified bootstrap test, whereas $\overline{SMC_{meas}}$ represents the average measured SMC value across the same set of bootstrap samples.

2.3. Inversion Process

The inversion procedure in the MARMIT model consists of two steps. The first step optimizes the thickness of the water level (L) and the fraction of the surface covered by water (e) by minimizing the difference between the predicted and measured reflectance of wet soil derived from hyperspectral imagery at different moisture levels. We used the Nelder–Mead simplex method in this instance, followed by the calibration step in which the optimized L and e are fit through the logistic functional form in Equation 8 to the SMC.

The (SWAP)-Hapke model incorporates a different three-step inversion procedure. In the first step, single scattering albedo (w), scale of the SHOE (B_{SD}) , the width of SHOE (h), and the coefficients of the SOILSPECT phase function (b,b',c,c') are optimized by minimizing the difference between the predicted reflectance of the SOILSPECT model and the measured reflectance of dry soil. The second step optimizes parameter L using the measured wet soil reflectance and the third step is the same calibration step in the MARMIT model. In the original (SWAP)-Hapke model described by G.-J. Yang et al. (2011), parameter optimization used the Powell-Ant Colony Algorithm. However, we employed the differential evolution algorithm (Storn & Price, 1997) in the first optimization process and in the second, the Nelder-Mead (Nelder & Mead, 1965), because of their better performance. To be consistent, we followed the same steps for our modified version of the (SWAP)-Hapke model. As implemented here, the only distinction in the optimization step between the (SWAP)-Hapke model and our modified (SWAP)-Hapke model (described above) is the number of free parameters. In our modified (SWAP)-Hapke model, we used the first algorithm (Differential Evolution Algorithm) to optimize eight parameters and the second (Nelder-Mead Algorithm) to optimize the remaining two (L and ϵ). Table 1 displays the parameters of each model and their respective range of possible values.

3. Experimental Design and Results

3.1. SMC Retrieval Using Laboratory Data

In the laboratory, we used four soil samples and associated BCRF measurements that were part of an earlier study (Eon & Bachmann, 2021b) that included sediment samples with varying physical features from four distinct locations. That earlier study focused solely on retrieval using the MARMIT model for these laboratory data and a more limited set of hyperspectral imagery collected over Hog Island from UAS systems (Eon & Bachmann, 2021b). One sample is from Algodones Dunes, California (ALG) that was part of another study (Bachmann, Eon, Ambeau, et al., 2018; McCorkel et al., 2017) there involving the NASA Goddard Light Detection And Ranging, Hyperspectral, and Thermal (G-LiHT) system (Cook et al., 2013). This sample is mainly composed of quartz and heavy minerals (Smith et al., 1984). Two samples are from Hog Island, Virginia (Bachmann, Eon, Lapszynski, et al., 2018; Eon et al., 2020). One of them is from the beach side with sandy sediment (HOGB), and

NUR AND BACHMANN 6 of 21

Parameters	Value range	MARMIT	Original (SWAP)-Hapke	Modified (SWAP)-Hapke
Thickness of water layer (L)	0–2	Free	Free	Free
Surface coverage fraction of water (ε)	0–1	Free	Fixed	Free
Single scattering albedo (w)	0–1	-	Free	Free
Scale of the SHOE (B_{S0})	0–1	-	Free	Free
Width of the SHOE (h)	0–1.5	-	Free	-
Fill factor(ϕ)	0-0.752	-	-	Free
Coefficient of the SHOE width (β)	0–1	-	-	Free
Coefficient of the SOILSPECT phase function (b)	-2-2	-	Free	
Coefficient of the SOILSPECT phase function (b')	-2-2	-	Free	
Coefficient of the SOILSPECT phase function (c)	-1-1	-	Free	
Coefficient of the SOILSPECT phase function (c')	-1-1	-	Free	-
Coefficient of the single scattering phase function (a_1)	-2-2	-	-	Free
Coefficient of the single scattering phase function (a_2)	-2-2	-	-	Free
Coefficient of the single scattering phase function (a_3)	-2-2	-	-	Free
Coefficient of the single scattering phase function (a_4)	-2-2	-	<u>-</u>	Free

the other one from a salt-panne (HOGP) environment (Eon et al., 2020), which consists primarily of clay, silt, and sand. The final sample that we analyzed in the laboratory was collected from a lakebed location in northwestern Nevada (G. Badura et al., 2019). This sample (NEV) is mainly composed of clay.

The BRF data used in this segment of our analysis was measured in our laboratory using a hyperspectral goniometer, the Goniometer of the Rochester Institute of Technology-Two (GRIT-T) (Harms et al., 2017) covering a range of moisture content from dry to fully saturated (Eon & Bachmann, 2021a, 2021b). The GRIT-T is a sophisticated goniometric system designed for use in field and laboratory settings and has seen widespread application in previous research (Bachmann, Eon, Ambeau, et al., 2018; G. Badura et al., 2019; G. Badura & Bachmann, 2019; G. P. Badura et al., 2019; Eon et al., 2018, 2020; Eon & Bachmann, 2021b; Roth et al., 2020, 2021; Shiltz & Bachmann, 2023). Users can create custom scan patterns to manage the system's arm, head, and carriage. A laser distance from the nadir is measured at the beginning of each scan to avoid parallax errors and ensure consistent measurements across various surface configurations. Equipped with a pair of Analytical Spectral Device FieldSpec Full-Range 4 (ASD FR4) spectroradiometers, the system records 2,151 spectral channels within the 350-2,500 nm range at 1 nm intervals, featuring a 3 nm spectral resolution in the visible and near-infrared (VNIR) region and an 8 nm resolution in the shortwave infrared (SWIR) region. In the field, one spectrometer can measure downwelling radiance while the other measures surface scattered radiance. Because of the absence of diffuse light in the laboratory environment, only the downward-looking spectrometer was used in the measurements described in this work. The raw data were initially converted to calibrated radiance, a process proficiently executed using the ASD ViewSpec Pro software (ViewSpec Pro Software, Accessed: 09 May 2023). The conversion from radiance to reflectance involves using a Spectralon™ panel's radiance measurement. In this study, our analysis was based on the bi-directional reflectance factor (BRF), which compares light scattering from a sample's surface at specific incident illumination and observation geometries with light scattering from a perfectly diffuse (Lambertian) surface. Because Spectralon™ white reference panels do not display ideal Lambertian reflectance characteristics, our Bi-directional Reflectance Factor (BRF) calculations incorporated the panel calibration coefficient. This strategy was designed to suitably account for the non-ideal Lambertian reflectance behavior presented by the Spectralon™ panel. The BRF calculation was carried out using the following formula:

$$BRF(\theta_i, \phi_i, \theta_r, \phi_r) = \frac{L_{Sample}(\theta_i, \phi_i, \theta_r, \phi_r)}{L_{SP}(\theta_i, \phi_i, \theta_r, \phi_r)} \cdot C_{SP}$$
(26)

where L_{Sample} , L_{SP} , C_{SP} , θ_i , ϕ_i , θ_r , and ϕ_r correspond to the sample radiance, SpectralonTM panel radiance, SpectralonTM panel calibration coefficient, incident zenith angle, incident azimuth angle, observation zenith angle, and observation azimuth angle respectively.

NUR AND BACHMANN 7 of 21

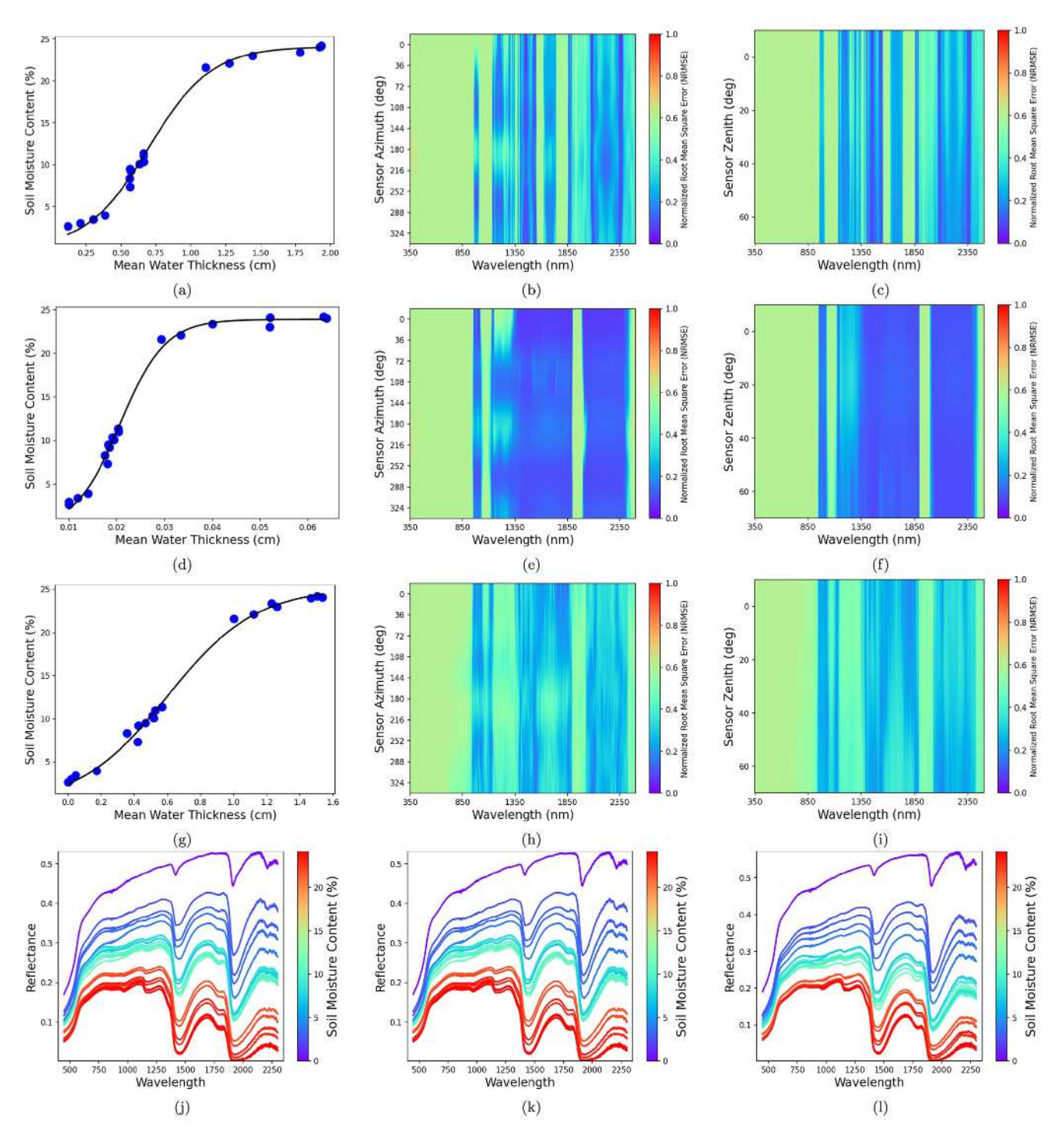


Figure 1. Model outputs: (row 1) MARMIT, (row 2) (SWAP)-Hapke, (row 3) modified (SWAP)-Hapke models using laboratory BRF of the Algodones Dunes (ALG) sample with various moisture levels: (a, d, g) plots show the relationship between soil moisture content (SMC) and mean water thickness (L) for the optimal model fit across all available combinations of wavelength and sensor zenith/azimuth orientations, (b, e, h) the normalized root mean squared error (NRMSE) as a function of sensor relative azimuth (averaged over all sensor zenith at that particular sensor azimuth) and wavelength, and (c, f, i) NRMSE as a function of sensor zenith (averaged over all sensor azimuth at that particular sensor zenith) and wavelength. (Last row: j, k, and l) spectra at the best-fit sensor geometry for the MARMIT, (SWAP)-Hapke, and modified (SWAP)-Hapke models, respectively, with varying moisture content levels.

NUR AND BACHMANN 8 of 21

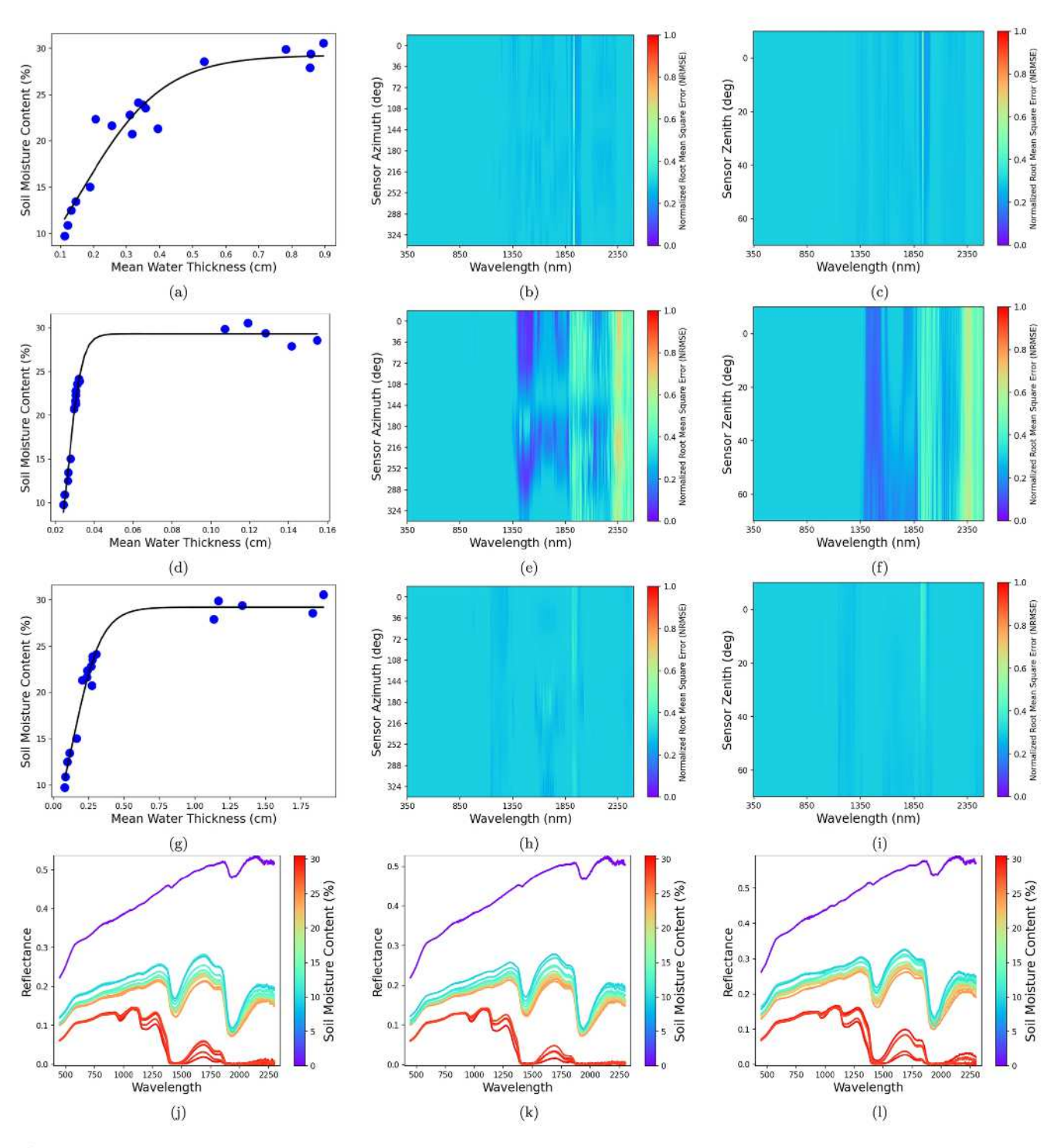


Figure 2. Model outputs: (row 1) MARMIT, (row 2) (SWAP)-Hapke, (row 3) modified (SWAP)-Hapke models using laboratory BRF of the Hog Island Beach (HOGB) sample with various moisture levels: (a, d, g) plots show the relationship between soil moisture content (SMC) and mean water thickness (L) for the optimal model fit across all available combinations of wavelength and sensor zenith/azimuth orientations, (b, e, h) the normalized root mean squared error (NRMSE) as a function of sensor relative azimuth (averaged over all sensor zenith at that particular sensor azimuth) and wavelength, and (c, f, i) NRMSE as a function of sensor zenith (averaged over all sensor azimuth at that particular sensor zenith) and wavelength. (Last row: j, k, and l) spectra at the best-fit sensor geometry for the MARMIT, (SWAP)-Hapke, and modified (SWAP)-Hapke models, respectively, with varying moisture content levels.

NUR AND BACHMANN 9 of 21

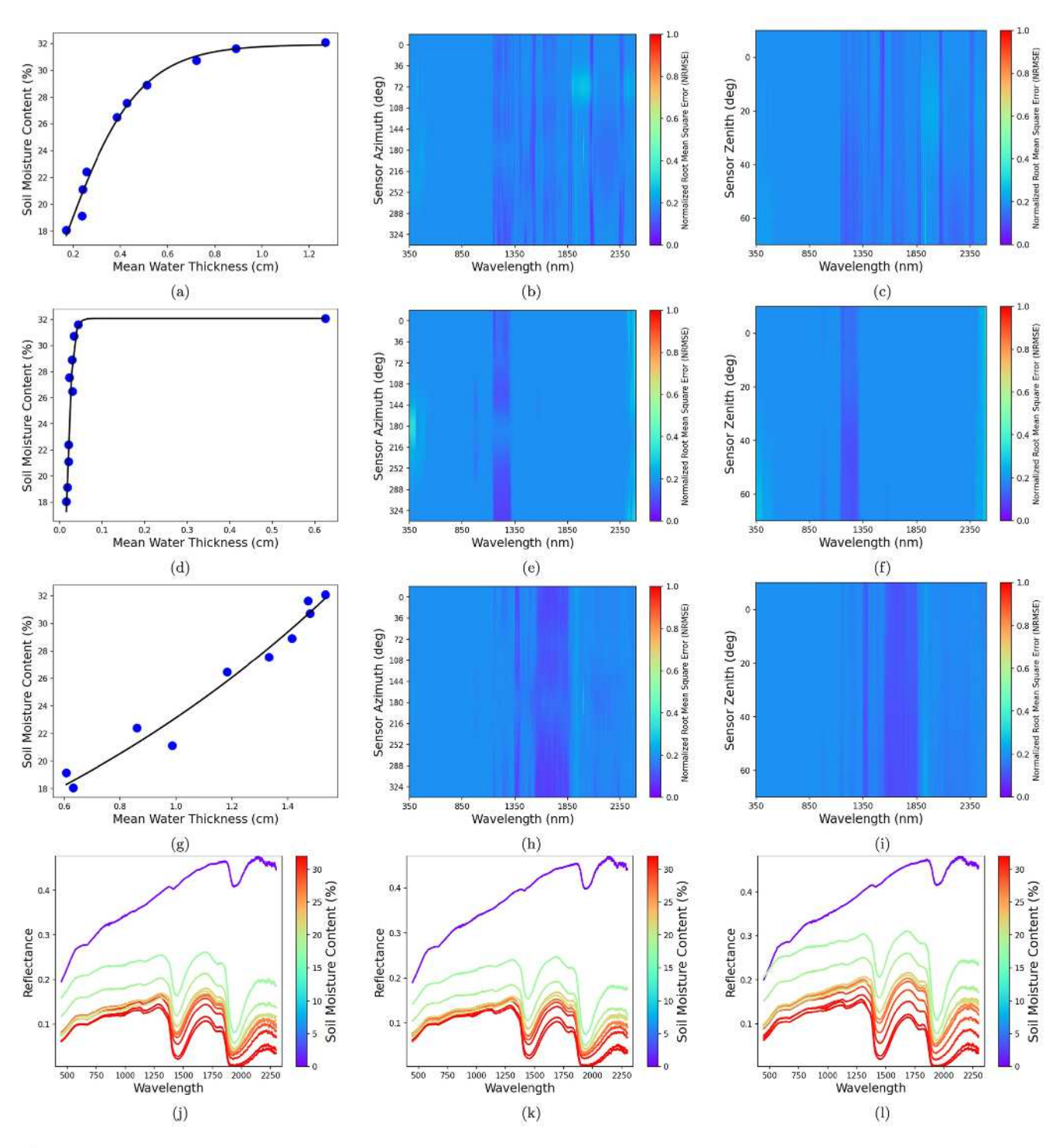


Figure 3. Model outputs: (row 1) MARMIT, (row 2) (SWAP)-Hapke, (row 3) modified (SWAP)-Hapke models using laboratory BRF of the Hog Island Panne (HOGP) sample with various moisture levels: (a, d, g) plots show the relationship between soil moisture content (SMC) and mean water thickness (L) for the optimal model fit across all available combinations of wavelength and sensor zenith/azimuth orientations, (b, e, h) the normalized root mean squared error (NRMSE) as a function of sensor relative azimuth (averaged over all sensor zenith at that particular sensor azimuth) and wavelength, and (c, f, i) NRMSE as a function of sensor zenith (averaged over all sensor azimuth at that particular sensor zenith) and wavelength. (Last row: j, k, and l) spectra at the best-fit sensor geometry for the MARMIT, (SWAP)-Hapke, and modified (SWAP)-Hapke models, respectively, with varying moisture content levels.

NUR AND BACHMANN 10 of 21

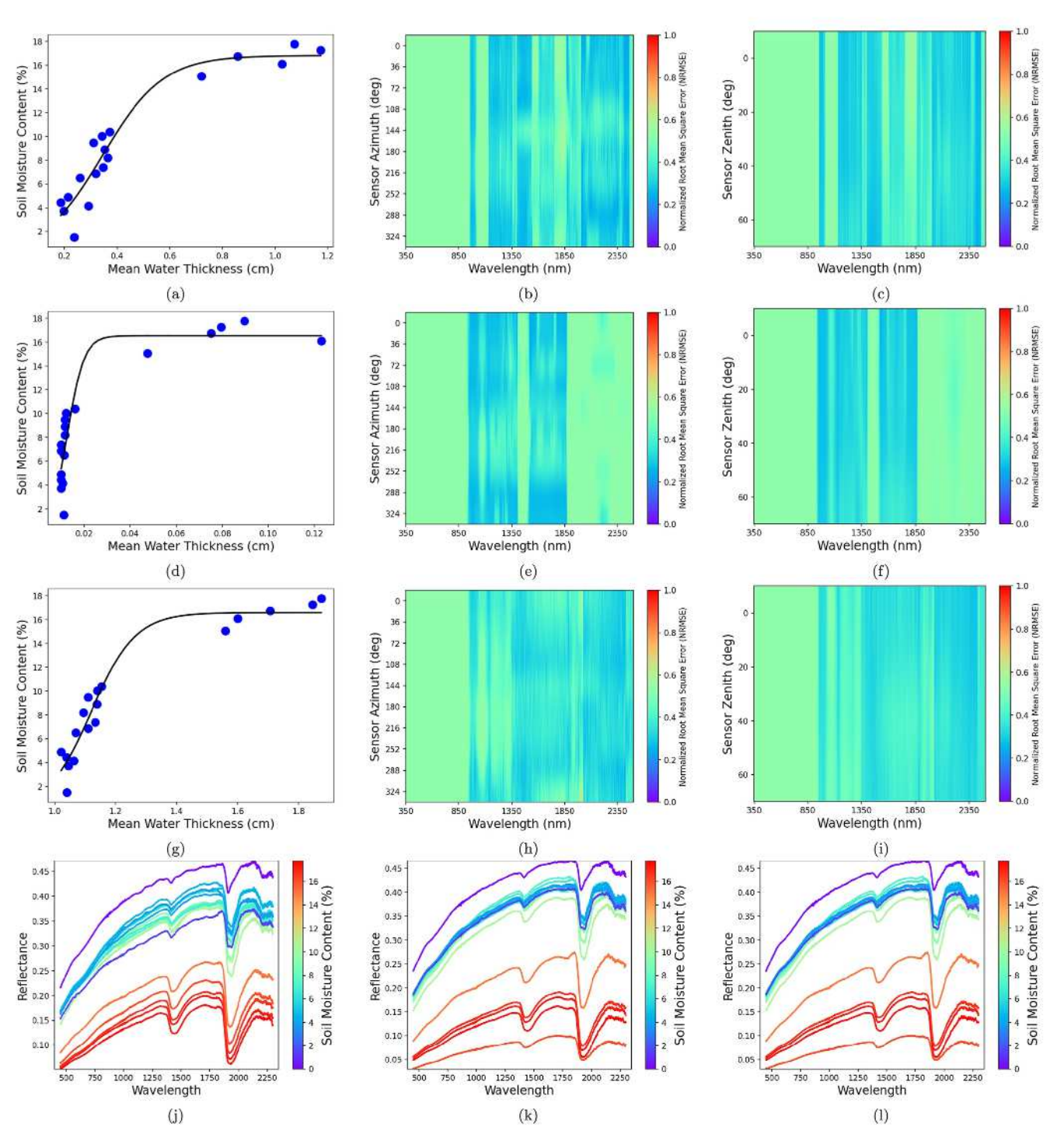


Figure 4. Model outputs: (row 1) MARMIT, (row 2) (SWAP)-Hapke, (row 3) modified (SWAP)-Hapke models using laboratory BRF of the Nevada (NEV) sample with various moisture levels: (a, d, g) plots show the relationship between soil moisture content (SMC) and mean water thickness (L) for the optimal model fit across all available combinations of wavelength and sensor zenith/azimuth orientations, (b, e, h) the normalized root mean squared error (NRMSE) as a function of sensor relative azimuth (averaged over all sensor zenith at that particular sensor azimuth) and wavelength, and (c, f, i) NRMSE as a function of sensor zenith (averaged over all sensor azimuth at that particular sensor zenith) and wavelength. (Last row: j, k, and l) spectra at the best-fit sensor geometry for the MARMIT, (SWAP)-Hapke, and modified (SWAP)-Hapke models, respectively, with varying moisture content levels.

NUR AND BACHMANN 11 of 21

ry.wiley.com/doi/10.1029/2023JG007381 by UNIVERSITY OF VIRGINIA, Wiley Online Library on [14/11/2023]. See the Terms and Com-

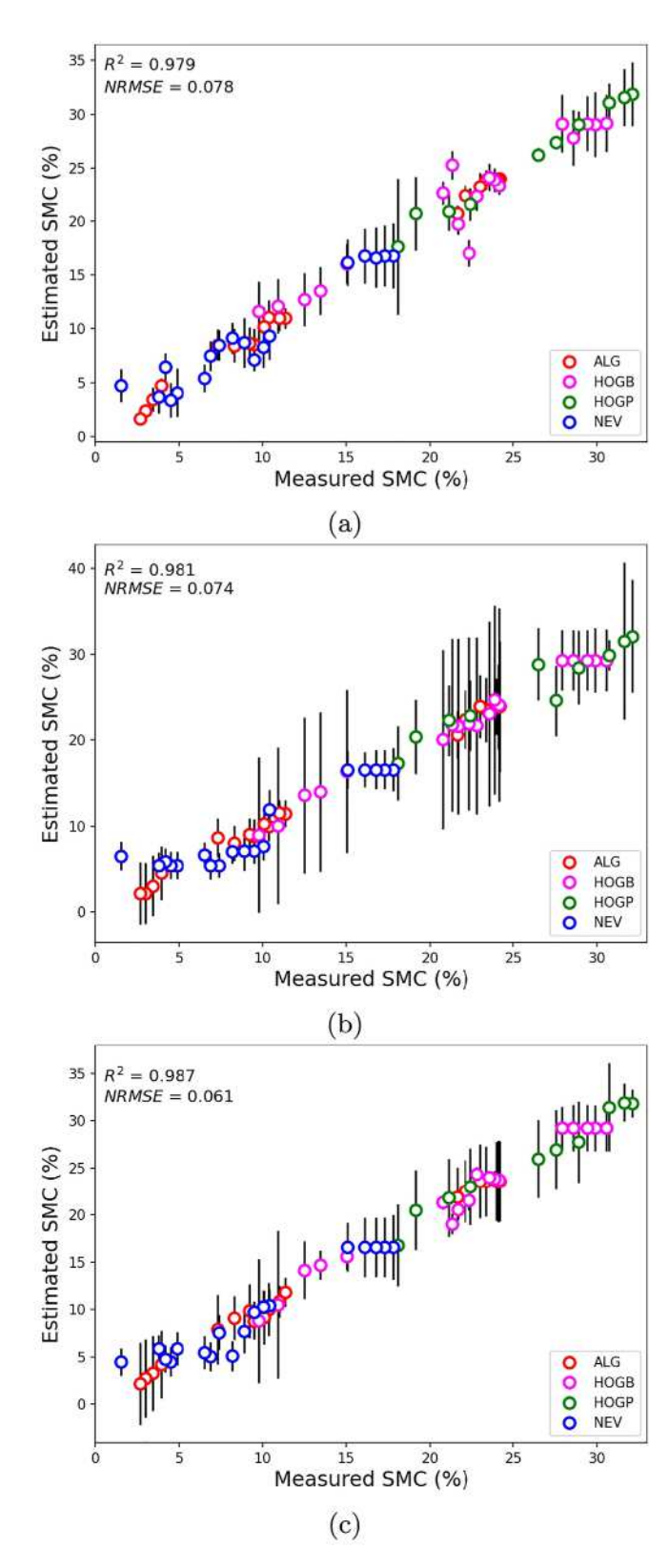


Figure 5. Retrieved SMC Estimate (%) versus measured SMC (%) for four types of laboratory samples (ALG, HOGB, HOGP, and NEV) using (a) MARMIT model, (b) (SWAP)-Hapke model, and (c) the modified (SWAP)-Hapke model.

Using a Cornell Sprinkle Infiltrometer (Van Es & Schindelbeck, 2003), the soil moisture content of the samples was varied to examine the influence on the observed BRF. The last row of Figures 1–4 depicts the variation in soil spectra as a function of the soil moisture content. When the soil is entirely dry, its reflectance is at its peak. As the amount of moisture increases, reflectance decreases. The two major water absorption bands centered at 1,440 nm and 1,930 nm exhibit the greatest variation in moisture content.

As all of our models estimate the mean equivalent water thickness, in order to retrieve SMC, it is essential to establish a link between mean equivalent water thickness and SMC. Therefore, we used Equation 8 (Bablet et al., 2018) for all models to determine coefficients of the logistic function. However, according to Bablet et al. (2018), it is not feasible to identify a general relationship between equivalent water thickness and SMC that applies to all sediment types. So, for each model, we obtained a unique logistic function for a unique sample type. The logistic function linking the SMC to the equivalent water thickness for each sediment type is shown in the first column of Figures 1–4, with the MARMIT, (SWAP)-Hapke, and modified (SWAP)-Hapke in the first, second, and third rows respectively. Table 2 displays the wavelength and sensor geometry at which the best model fit was discovered. The illumination zenith angle for all laboratory BRF spectral data collection was 40°.

The second and third columns of the first three rows of Figures 1–4 depict the NRMSE for each sediment sample as a function of sensor azimuth (averaged over all sensor zenith) and zenith (averaged over all sensor azimuth) for the entire wavelength range (350–2,500 nm), again with the MARMIT, (SWAP)-Hapke, and modified (SWAP)-Hapke in the first, second, and third rows respectively. Although we chose the sensor geometry and the band that produced the lowest NRMSE (Table 2), Figures 1–4 show that wavelengths corresponding to water absorption bands offer reliable results across a wide range of geometries. The spectra at the best-fit sensor geometry for the MARMIT, (SWAP)-Hapke, and modified (SWAP)-Hapke models, with varied moisture content levels, are shown in the last row of Figures 1–4.

Figure 5 depicts a scatter plot of the measured SMC versus the predicted SMC for all sediment samples from the laboratory-measured BRF data. The circles represent the best-matched moisture obtained across all sensor zenith and azimuth measurements and wavelength combinations. The error bar indicates the variance between the true SMC and model-estimated SMC across all sensor zenith and azimuth directions at the best-fitted wavelength. When comparing the performance of modified and original (SWAP)-Hapke models, we found that the relative performance of these models varied when applied to different samples. However, when combined, as in Figure 5, the modified (SWAP)-Hapke model exhibits slightly better performance. The regression coefficient of determination, R2 (Olofsson & Andersson, 2012), and normalized mean square error, NRMSE, for all samples are, respectively, (0.979, 0.981, 0.987) and (0.078, 0.074, 0.061) for MARMIT, (SWAP)-Hapke, and the modified (SWAP)-Hapke models. Thus, the lowest NRMSE and best R^2 goodness of fit were obtained with the modified (SWAP)-Hapke model. For the MARMIT and original (SWAP)-Hapke models, the R^2 and NRMSE values are comparable, both with lower R^2 and higher NRMSE than the modified (SWAP)-Hapke model.

NUR AND BACHMANN 12 of 21

Model Outputs	Usino I	aboratory	Hyperspectral	Imaoerv
model Outputs	osing L	моониогу.	пуретърести	imager y

			Best fit obser	ved		Logistic function parameters for the best fit			
Model	Sample	Wavelength (nm)	Sensor zenith (deg)	Sensor azimuth (deg)	r^2	A	В	Ψ	
MARMIT	ALG	2,082.0	60.0	36.0	0.995	24.07	4.49	23.045	
	HOGB	1,572.0	0.0	72.0	0.918	29.250	8.039	3.742	
	HOGP	1,550.0	20.0	108.0	0.985	31.919	6.126	2.289	
	NEV	1,320.0	40.0	324.0	0.925	16.827	8.735	20.334	
(SWAP)-Hapke	ALG	2,422.0	60.0	36.0	0.995	23.905	213.506	83.873	
	HOGB	2,053.0	0.0	0.0	0.985	29.297	297.578	2,996.03	
	HOGP	2,473.0	32.081	138.545	7.549				
	NEV	1,540.0	1,540.0 40.0 0.0 0.866					37.486	
Modified	ALG	950.0	125,976,250.49	1.35	79,538,181.83				
(SWAP)-Hapke	HOGB	1,667.0	60.0	288.0	0.974	29.233	7.658	6.277	
	HOGP	2,422.0	60.0	252.0	0.972	39.384	2.079	12.229	
	NEV	2,417.0	40.0	0.0	0.923	16.598	11.429	13.345	

While this result suggests the possibility of improved performance for the (SWAP)-Hapke model, a more realistic test using UAS hyperspectral imagery constituted the next phase of our analysis, and some critical differences exist between the laboratory setting, which only employs a directional source, compared to the field setting, where both direct solar illumination and diffuse skylight illumination are present. In the next section, we describe a bootstrap statistical analysis of results obtained from these three models for UAS-based hyperspectral imagery.

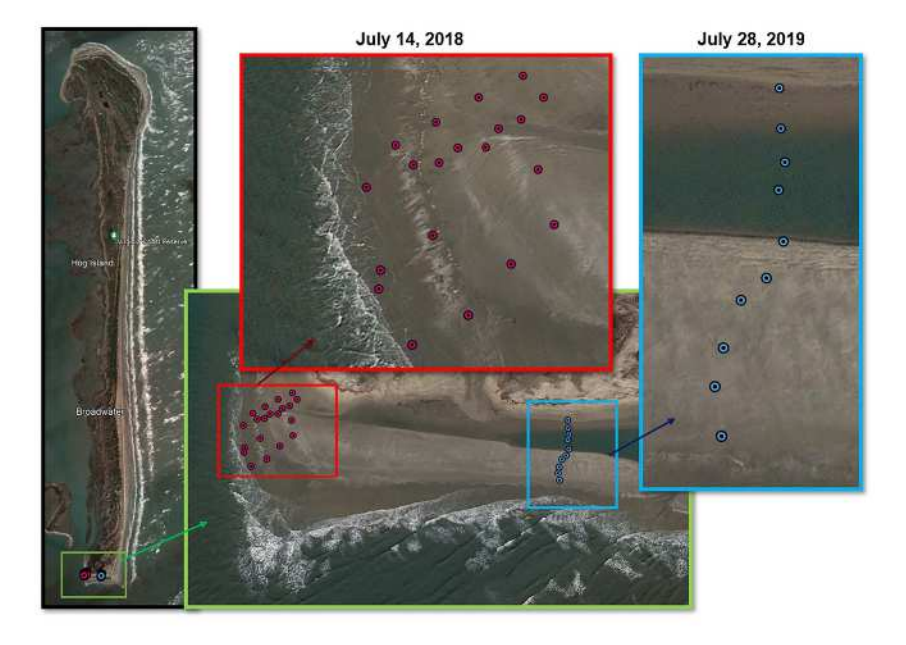
3.2. SMC Retrieval Using UAS Data

The hyperspectral imagery and coincident field ground truth data were collected on Hog Island, a barrier island located at 37° 25′ 5.91″ N, 75° 41′ 36.71″ W. The island is part of the Virginia Coast Reserve Long Term Ecological Research (VCR-LTER) site (Virginia Coast Reserve Long Term Ecological Research site, Accessed: 09 May 2023). It is roughly 10 km long and 2.5 km wide and is located 14 km off the coast of the mainland. This island has been the subject of intensive ecological and geological studies (Bachmann et al., 2002, 2003; McLoughlin et al., 2015; Osgood & Zieman, 1993; Tyler et al., 2003; Tyler & Zieman, 1999; Young et al., 2007). During field campaigns in 2018 and 2019, we acquired both ground truth (SMC and other geophysical data) and contemporaneous hyperspectral imagery along the shoreline of the southern point of Hog Island, Virginia, utilizing UAS-based hyperspectral imaging systems. The multi-sensor UAS payloads (Kaputa et al., 2019) incorporated two HSI systems: a Headwall Nano-Hyperspec with 270 visible and near-infrared (400–1,000 nm) spectral bands and a Headwall Micro-Hyperspec High Efficiency (Micro-HE) with 267 short-wave infrared (SWIR) spectral bands (900–2,500 nm). Based on our laboratory studies, for all the models that we previously discussed, numerous wavelengths with moderately low NRMSE appropriate for recovering SMC with high precision appear in the SWIR spectral range. Therefore, we opted to employ just SWIR hyperspectral imaging to execute the inversion of the three radiative transfer models for SMC.

The SWIR Micro-HE hyperspectral imaging system specifications include 267 spectral bands within the range of 900–2,500 nm, 384 spatial bands, a 24 μm pixel pitch, and a 16-bit analog-to-digital conversion. The system exhibits a peak signal-to-noise ratio (SNR) of 350:1 at around 1,250 nm wavelength. This SNR value was computed with calibration data gathered via a 0.5-m LabSphere Helios 20 integrating sphere and a 3000K quartz tungsten halogen light source in strict compliance with EMVA Standard 1288, a benchmark for characterizing image sensors and cameras (EMVA Standard 1,288, Accessed: 09 May 2023). In the context of field calibration, we strategically deployed three calibration panels: light gray, dark gray, and black. Each panel's well-documented ground truth radiance was acquired, facilitating its role in the calibration process. Concurrently, we measured the radiance of a SpectralonTM plaque under identical illumination conditions just before flight. Leveraging Equation 26, we calculated the ground truth reflectance of these three calibration panels. The hyperspectral imagery,

NUR AND BACHMANN 13 of 21

21698961, 2023. 6, Downloaded from https://agupubs.onlinelibrary.wiley.com/doi/10.1029/2023/G007381 by UNIVERSITY OF VIRGINIA, Wiley Online Library on [14/11/2023]. See the Terms and Conditions



(a)

Figure 6. (a) Hog Island beach study area from Google Earth indicating ground truth locations for UAS hyperspectral imagery collected on 14 July 2018 (red circles), and 28 July 2019 (blue circles). (b) UAS hyperspectral imaging system capturing imagery of beach regions with different SMC levels on 28 July 2019. The stakes are the locations of some of the ground truth positions.

(b)

captured in the field using the UAS-mounted SWIR hyperspectral imaging system, was initially orthorectified and converted to radiance using Headwall's Hyperspec III SpectralView software (Hyperspectral and Operational Software, Accessed: 09 May 2023). The spectra of the calibration panels were then extracted using the ENVI software (Version 5.6.2) (L3Harris ENVI, Accessed: 09 May 2023). Subsequently, we determined the relationship between the calibration panels' ground truth reflectance and their UAS-acquired radiance spectra

NUR AND BACHMANN 14 of 21

Date	Flight name	Average solar zenith(deg)	Average solar azimuth(deg)	Number of visible SMC ground truth positions
14 July 2018	Mission-1216	18.49	145.41	19
	Mission-1347	18.27	213.32	10
	Mission-1541	38.68	257.69	19
28 July 2019	Mission-0950	46.22	99.51	10
	Mission-1019	40.73	105.09	10
	_			Total = 68

using the empirical line method within the ENVI software (ENVI: Atmospheric Correction via Empirical Line Method, Accessed: 09 May 2023). This established relationship, an empirical line method fit, was then applied to convert radiance to reflectance for each wavelength. This rigorous calibration process ensures the uniformity and comparability of reflectance data derived from radiance measurements, regardless of the date, sensor, or environmental condition.

In this analysis, we have utilized SMC ground truth data sets collected on two different days: one set is from 14 July 2018, and the other is from 28 July 2019 (see Figure 6). Each of these days had multiple drone flights throughout the day (see Table 3 for details). We aimed to gather data from as many flights as possible to include a relatively wide range of sensor and solar geometries. By incorporating hyperspectral imagery with an extensive range of sensor and solar geometries, our statistical bootstrap tests provide a more thorough understanding of model performance. In our analysis, we utilized a subset of five drone flights in total, which allowed us to observe a single sample from different angles. As these scans were conducted throughout the day, the variation in solar angle also allowed us to evaluate the performance of each model with varying solar elevation.

We conducted a bootstrap analysis consisting of 1,000 iterations to evaluate the performance of each soil moisture content (SMC) retrieval model described in Section 2. For each iteration, we chose at random a subset of the available field measurements of soil moisture content (SMC) and reflectance data for training (80% of the data) and testing (20% of the data). For each iteration, first, we recorded the wavelength and model parameters that resulted in the highest agreement between the predicted and ground truth SMC when using training data. Then, we used that trained model to predict SMC for the test data set. Finally, after all those 1,000 iterations, we chose the wavelength that consistently gave the best results for the training data and used the logistic parameters for that wavelength to map the SMC, as shown in Figure 8 and to evaluate the specific sample positions set aside for testing in the bootstrap iteration.

Figure 7 and Table 4 illustrate the bootstrap results for each model when using the UAS hyperspectral imagery. The histograms in the first row are the NRMSE of 1,000 bootstrap tests. The logistic function plot of each model at the wavelength where the best fit was observed the maximum number of times is shown in the second row of Figure 7. The results of just one bootstrap test near the histogram mean are displayed in the third and fourth rows. It is apparent from the first-row histogram plots that MARMIT performs better than the other models when using the UAS data. Both the mean and median NRMSE are smaller than those of the competing models. This may occur for various reasons, which are discussed in Section 4.

4. Discussion

From the results for the single best model over all wavelengths and view geometries reported in Table 2, we saw that MARMIT and the original (SWAP)-Hapke model obtained similar performance for laboratory BRF data. Our proposed modified version of the (SWAP)-Hapke model performed marginally better than the other two models for these data. However, when utilizing UAS hyperspectral imagery, our model continues to perform better than the original (SWAP-Hapke) model but does not surpass MARMIT. Differences in the underlying assumptions of these models likely play a role in these outcomes. Both the original (SWAP)-Hapke model (G.-J. Yang et al., 2011) and our modified version use Hapke's radiative transfer model (Hapke, 1981, 2012) to predict

NUR AND BACHMANN 15 of 21

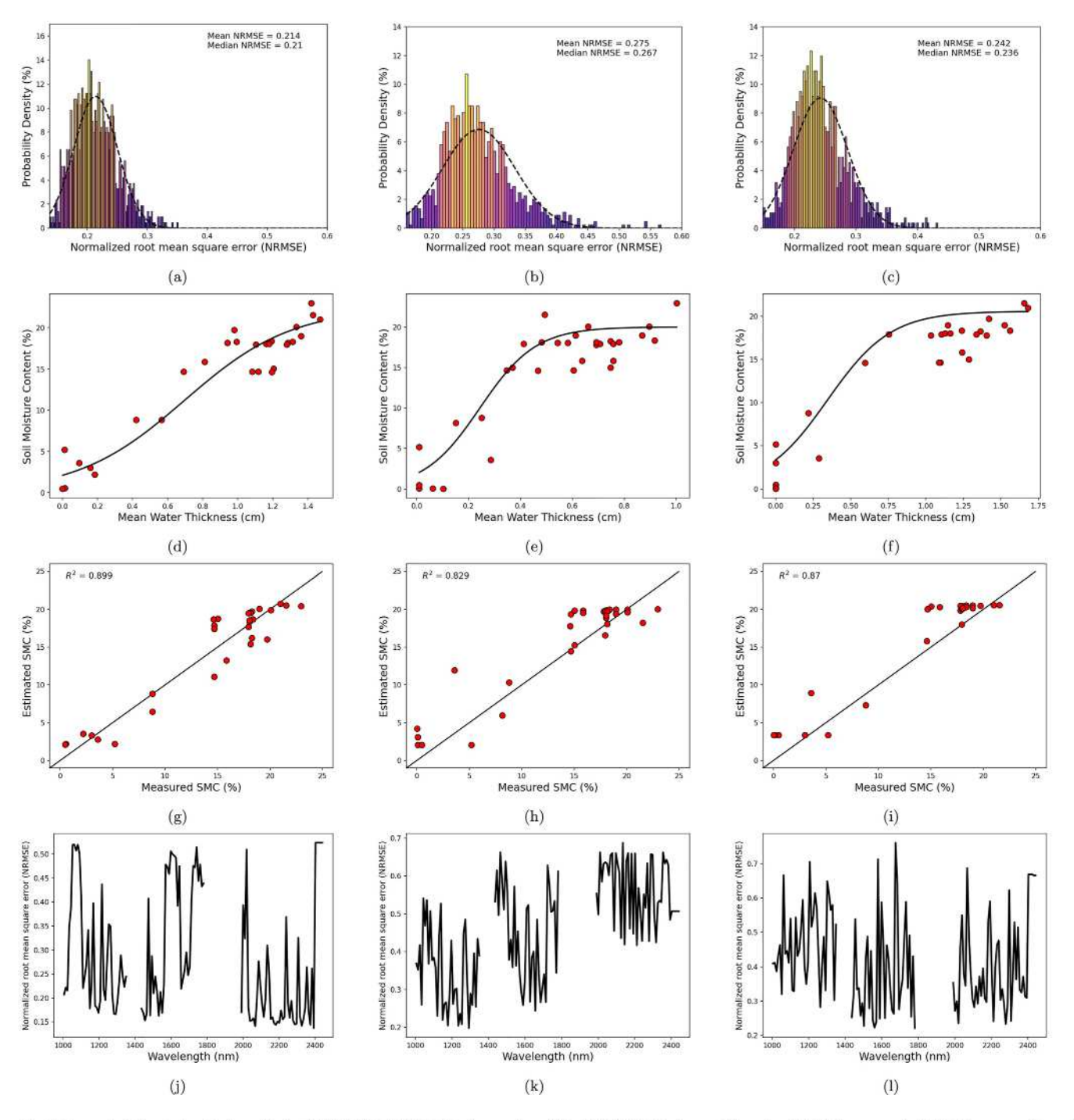


Figure 7. Columns 1–3: bootstrap test results for MARMIT, (SWAP)-Hapke, and modified (SWAP)-Hapke models using SWIR hyperspectral UAS imagery. (Row 1) histogram of each model's NRMSE value over 1,000 bootstrap tests. Each bootstrap test randomly selected 80% of the data for calibration and 20% for testing. (Row 2) optimized logistic function plots for each model at the wavelength where the best fit was observed the maximum number of times. (Row 3) model estimated SMC versus measured SMC for one of the bootstrap tests near histogram mean. (Row 4) NRMSE as a function of wavelength for that particular bootstrap test.

the SMC, and the underlying Hapke IMSA model is based on the assumption of a directional source and includes a more comprehensive treatment of multiple scattering interactions, although in an isotropic manner, at least within the assumed separate soil layer. MARMIT has a more limited treatment of multiple scattering, but does provide for interactions between the equivalent water layer, the soil layer, and the air, and, in particular treats the internal reflection and transmission at the air-water boundary using a diffuse illumination model. In the labora-

NUR AND BACHMANN 16 of 21

onlinelibrary.wiley.com/doi/10.1029/2023JG007381 by UNIVERSITY OF VIRGINIA, Wiley Online Library on [14/11/2023]. See the Terms

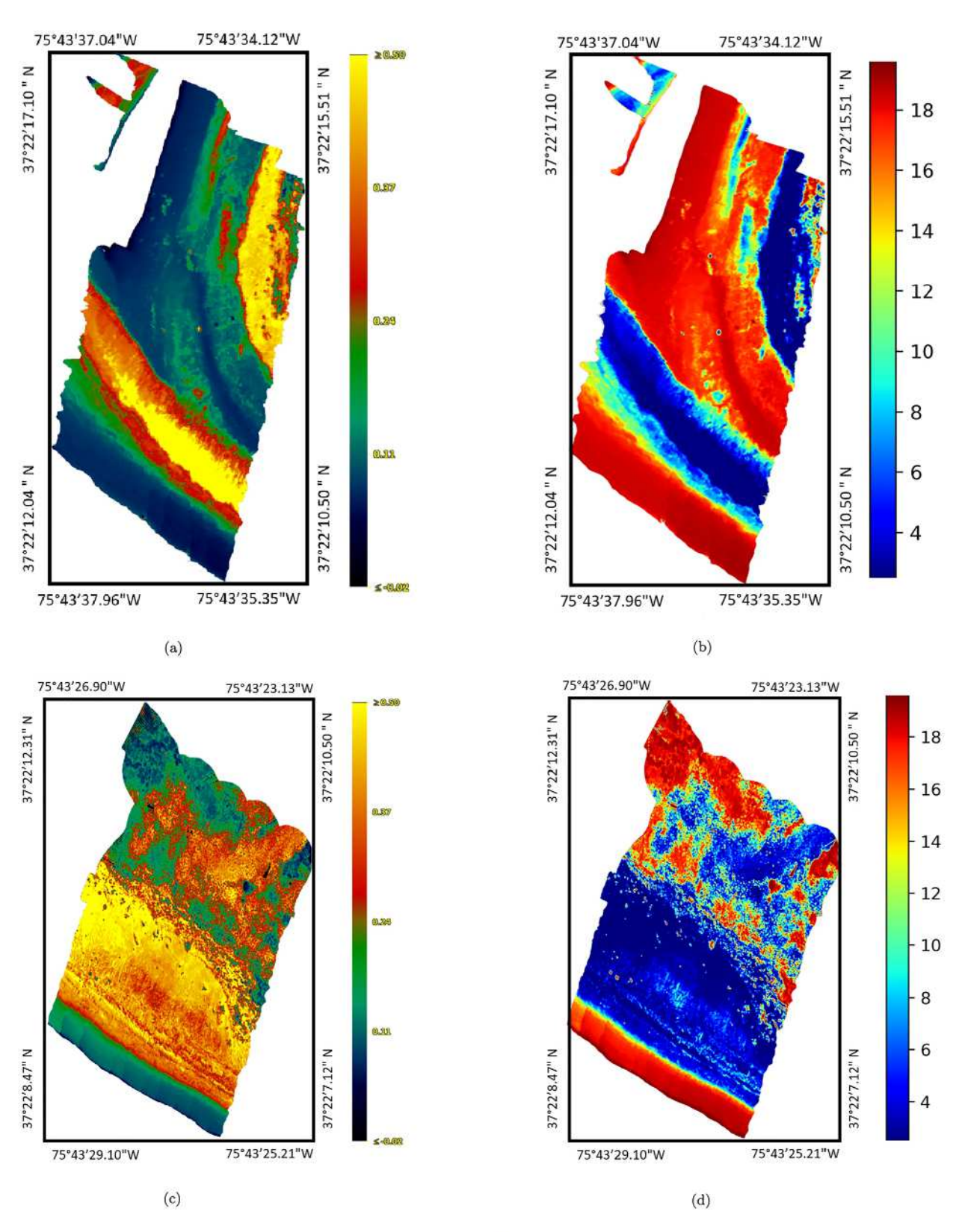


Figure 8. (a) Single band (2,192.35 nm) reflectance, the best-fit wavelength in Table 4, and (b) retrieved SMC percentage using the MARMIT model over the entire 2018 beach study region on the southern end of Hog Island on 14 July 2018. (c) Single band (2,192.35 nm) reflectance and (d) retrieved SMC percentage using the MARMIT model over the entire 2019 beach study region on the southern end of Hog Island on 28 July 2019.

NUR AND BACHMANN 17 of 21

¥ .684 .638

tanne +												
Model Outputs for 1,000 Bootstrap Tests Using UAS Hyperspectral Imagery	tstrap Tests Using	UAS Hypersp.	ectral Imagery	у								
	Best fit observed at	Magn 22		Median "2		Maximum v2	Minimim	St day 22	St dev	Logistic function paramete for results closest to mean value	nction para closest to n value	mete
Model	(nm)	value	NRMSE	value	NRMSE	value	NRMSE	value	NRMSE	Ą	В	_
MARMIT	2,192.35	0.899	0.214	0.903	0.21	0.953	0.138	0.029	0.036	20.4	3.255	9.6
(SWAP)-Hapke	1,292.54	0.829	0.275	0.847	0.267	0.952	0.16	0.075	0.058	20.022	9.291	9.6
Modified (SWAP)-Hapke	2,211.5	0.87	0.242	0.88	0.236	0.962	0.149	0.049	0.044	20.6	4.742	5

tory data with a directional source, the relative advantages and disadvantages of the MARMIT and the original (SWAP)-Hapke appear to lead to comparable performance. However, the modified (SWAP)-Hapke model used a more accurate version of the *H*-functions that describes multiple scattering in the underlying IMSA model as well as the porosity function included in later versions of IMSA, and for the directional illumination in the laboratory setting, obtained the best fit, likely as a result of these particular model improvements.

However, in the analysis of the UAS-hyperspectral imagery, the diffuse and directional nature of the illumination found in the field setting altered the advantage in favor of the MARMIT model. This is likely due to the previously mentioned component of MARMIT that includes internal reflection and transmission at the air-water boundary for multiply-scattered light coming from the equivalent water layer treated in a diffuse manner within MARMIT. Specifically, as noted earlier, this component of the model assumes a hemispherically averaged transmission and reflection at this boundary as originally described by Lekner and Dorf (1988) and Stern (1961). There is no such interaction term present in (SWAP)-Hapke or the modified version that we have proposed in this work. Instead, the water component of these models is a simple Beer-Lambert absorption model. It is likely that these differences lead to the better average performance of MARMIT in the case of combined directional and diffuse illumination associated with the UAS hyperspectral bootstrap tests. It is worth noting that, while data was collected from a range of sensor geometries in the laboratory setting, the data obtained from unmanned aerial systems (UAS) exhibit a more constrained sensor geometry. Additionally, the solar and sensor geometry of NASA SBG satellite imagery may be similarly restricted. These limitations in geometry can inevitably impact the quality of the best fit. However, it appears that the effect of the absence of diffuse illumination in the original and modified (SWAP)-Hapke model is the more significant factor in relative model performance. While these intercomparisons are for the best model found over wavelength and viewing geometry, as noted earlier, the plots showing NRMSE averaged over zenith angle and NRMSE average over azimuth angle in Figures 1-4 suggest that there is a range of wavelengths where typical NRMSE is low in one or more of the model types for each laboratory sample considered. This is of practical importance for application to satellite imagery in future development of global SMC retrieval models using hyperspectral imagery from future missions such as SBG.

5. Conclusions

We have described and intercompared three approaches to retrieving soil moisture content from hyperspectral imagery. All three models achieved good accuracy, with the best performance obtained with a directional laboratory source using our proposed modified version of the (SWAP)-Hapke model, while for UAS hyperspectral imagery, the MARMIT model achieved the best average performance. Specific differences in underlying modeling assumptions related to the treatment of multiple scattering either in the equivalent water layer or in the soil itself likely lead to these observed differences in performance between the directional-source illumination of the laboratory versus the combined directional solar and diffuse skylight illumination for the UAS hyperspectral imagery. The results of both the field and laboratory hyperspectral tests, that highlight these differences, suggest the possibility of exploring a new model which uses advantages derived from each approach. Since all models performed well in their present form, particularly in a realistic field test using data obtained from a UAS across more than one field campaign, this suggests that models of the types described here, or an improved model derived from the best features of each, could be used successfully with hyperspectral imagery from the future NASA SBG satellite mission. A successful SMC retrieval model based on the results described here could be used to develop a high-quality global SMC product using SBG hyperspectral imagery.

NUR AND BACHMANN 18 of 21

elibrary.wiley.com/doi/10.1029/2023JG007381 by UNIVERSITY OF VIRGINIA, Wiley Online Library on [14/11/2023]. See the Terms

on Wiley Online Library for rules of use; OA articles are governed by the applicable Creative

Data Availability Statement

The relevant laboratory and Unmanned Aerial System (UAS) datasets, in conjunction with the Python code for soil moisture retrieval models, are publicly available at Zenodo via DOI: https://doi.org/10.5281/zenodo.8021935 (Nur & Bachmann, 2023). To access the most recent updates, please visit our GitHub repository at: https://github.com/grit-lab/grit-lab-public-soil-moisture-retrieval-repo.

Acknowledgments

We gratefully acknowledge the field team members who worked with co-author CMB to collect the ground truth data and imagery on Hog Island used in this study: Rehman S. Eon, Christopher S. Lapszynski, Charles Tabor, and drone pilot Timothy Bauch. We would also like to acknowledge the use of the RIT Research High-Performance Computing Cluster (Rochester Institute of Technology, 2023) for the computation and analysis of the data presented in this article. We are grateful for the support and resources provided by the RIT Research Computing team. In addition. we would like to express our appreciation to David Conran, who kindly provided essential calibration information for the instruments used in our study. Finally, we would like to acknowledge and express our appreciation for the support provided by NSF DEB Grants #1237733 and #1832221 (VCR-LTER), which contributed to the execution of the fieldwork discussed in this study.

References

- Ambartsumian, V. (1944). On the problem of diffuse reflection of light. Journal of Physics-USSR, 8(1), 65.
- Ångström, A., & Angstrom, A. (1925). The albedo of various surfaces of ground. Geografiska Annaler, 7(4), 323–342. https://doi. org/10.2307/519495
- Babaeian, E., Sadeghi, M., Jones, S. B., Montzka, C., Vereecken, H., & Tuller, M. (2019). Ground, proximal, and satellite remote sensing of soil moisture. Reviews of Geophysics, 57(2), 530–616. https://doi.org/10.1029/2018rg000618
- Bablet, A., Viallefont-Robinet, F., Jacquemoud, S., Fabre, S., & Briottet, X. (2020). High-resolution mapping of in-depth soil moisture content through a laboratory experiment coupling a spectroradiometer and two hyperspectral cameras. *Remote Sensing of Environment*, 236, 111533. https://doi.org/10.1016/j.rse.2019.111533
- Bablet, A., Vu, P., Jacquemoud, S., Viallefont-Robinet, F., Fabre, S., Briottet, X., et al. (2018). MARMIT: A multilayer radiative transfer model of soil reflectance to estimate surface soil moisture content in the solar domain (400–2500 nm). *Remote Sensing of Environment*, 217, 1–17. https://doi.org/10.1016/j.rse.2018.07.031
- Bach, H., & Mauser, W. (1994). Modelling and model verification of the spectral reflectance of soils under varying moisture conditions. In Proceedings of IGARSS'94-1994 IEEE international geoscience and remote sensing symposium (Vol. 4, pp. 2354–2356).
- Bachmann, C. M., Bettenhausen, M. H., Fusina, R. A., Donato, T. F., Russ, A. L., Burke, J. W., et al. (2003). A credit assignment approach to fusing classifiers of multiseason hyperspectral imagery. *IEEE Transactions on Geoscience and Remote Sensing*, 41(11), 2488–2499. https://doi.org/10.1109/tgrs.2003.818537
- Bachmann, C. M., Donato, T. F., Lamela, G. M., Rhea, W. J., Bettenhausen, M. H., Fusina, R. A., et al. (2002). Automatic classification of land cover on smith island, VA, using HyMAP imagery. *IEEE Transactions on Geoscience and Remote Sensing*, 40(10), 2313–2330. https://doi.org/10.1109/ters.2002.804834
- Bachmann, C. M., Eon, R., Ambeau, B., Harms, J., Badura, G., & Griffo, C. (2018). Modeling and intercomparison of field and laboratory hyperspectral goniometer measurements with G-LiHT imagery of the algodones dunes. *Journal of Applied Remote Sensing*, 12(1), 012005. https://doi.org/10.1117/1.jrs.12.012005
- Bachmann, C. M., Eon, R. S., Lapszynski, C. S., Badura, G. P., Vodacek, A., Hoffman, M. J., et al. (2018). A low-rate video approach to hyperspectral imaging of dynamic scenes. *Journal of Imaging*, 5(1), 6. https://doi.org/10.3390/jimaging5010006
- Badura, G., & Bachmann, C. M. (2019). Assessing effects of azimuthally oriented roughness on directional reflectance of sand. Ieee Journal of Selected Topics in Applied Earth Observations and Remote Sensing, 12(3), 1012–1025. https://doi.org/10.1109/jstars.2019.2896592
- Badura, G., Bachmann, C. M., Harms, J., & Abelev, A. (2019a). Observed relationship between BRF spectral-continuum variance and macro-scopic roughness of clay sediments. *IEEE Transactions on Geoscience and Remote Sensing*, 57(9), 6726–6740. https://doi.org/10.1109/tgrs.2019.2908170
- Badura, G. P., Bachmann, C. M., Tyler, A. C., Goldsmith, S., Eon, R. S., & Lapszynski, C. S. (2019b). A novel approach for deriving LAI of salt marsh vegetation using structure from motion and multiangular spectra. *Ieee Journal of Selected Topics in Applied Earth Observations and Remote Sensing*, 12(2), 599–613. https://doi.org/10.1109/jstars.2018.2889476
- Berg, A., & Sheffield, J. (2018). Soil moisture-evapotranspiration coupling in CMIP5 models: Relationship with simulated climate and projections. *Journal of Climate*, 31(12), 4865–4878. https://doi.org/10.1175/jcli-d-17-0757.1
- Bonakdar, L., Oumeraci, H., & Etemad-Shahidi, A. (2016). Run-up on vertical piles due to regular waves: Small-scale model tests and prediction formulae. Coastal Engineering, 118, 1–11. https://doi.org/10.1016/j.coastaleng.2016.08.008
- Chahl, J. (2015). Unmanned aerial systems (UAS) research opportunities. *Aerospace*, 2(2), 189–202. https://doi.org/10.3390/aerospace2020189 Chandrasekhar, S. (1960). *Radiative transfer*. Dover.
- Ciarniello, M., Capaccioni, F., Filacchione, G., Clark, R. N., Cruikshank, D., Cerroni, P., et al. (2011). Hapke modeling of Rhea surface properties through Cassini-VIMS spectra. Icarus, 214(2), 541–555. https://doi.org/10.1016/j.icarus.2011.05.010
- Cook, B. D., Corp, L. A., Nelson, R. F., Middleton, E. M., Morton, D. C., McCorkel, J. T., et al. (2013). NASA Goddard's Lidar, hyperspectral and thermal (G-LiHT) airborne imager. Remote Sensing, 5(8), 4045–4066. https://doi.org/10.3390/rs5084045
- Domingue, D., & Hapke, B. (1989). Fitting theoretical photometric functions to asteroid phase curves. *Icarus*, 78(2), 330–336. https://doi.org/10.1016/0019-1035(89)90181-4
- Domingue, D., & Verbiscer, A. (1997). Re-analysis of the solar phase curves of the icy Galilean satellites. *Icarus*, 128(1), 49–74. https://doi.org/10.1006/icar.1997.5730
- Dong, J., Crow, W. T., Tobin, K. J., Cosh, M. H., Bosch, D. D., Starks, P. J., et al. (2020). Comparison of microwave remote sensing and land surface modeling for surface soil moisture climatology estimation. *Remote Sensing of Environment*, 242, 111756. https://doi.org/10.1016/j.
- EMVA standard 1288. (2023). Retrieved from https://www.emva.org/wp-content/uploads/EMVA1288-General-4.0ReleaseCandidate.pdf
- ENVI: Atmospheric correction via empirical line method. (2023). Retrieved from https://www.l3harrisgeospatial.com/docs/atmosphericcorrection.html#empirical_line_calibration
- Eon, R. S., & Bachmann, C. M. (2021a). The BCRF dataset used for mapping barrier island soil moisture using a radiative transfer model of hyperspectral imagery from an unmanned aerial system [Dataset]. UK AIR. https://doi.org/10.35009/cfccis-7c48
- Eon, R. S., & Bachmann, C. M. (2021b). Mapping barrier island soil moisture using a radiative transfer model of hyperspectral imagery from an unmanned aerial system. Scientific Reports, 11(1), 1–11. https://doi.org/10.1038/s41598-021-82783-3
- Eon, R. S., Bachmann, C. M., & Gerace, A. D. (2018). Retrieval of sediment fill factor by inversion of a modified Hapke model applied to sampled HCRF from airborne and satellite imagery. *Remote Sensing*, 10(11), 1758. https://doi.org/10.3390/rs10111758
- Eon, R. S., Bachmann, C. M., Lapszynski, C. S., Tyler, A. C., & Goldsmith, S. (2020). Retrieval of sediment filling factor in a salt Panne from multi-view hyperspectral imagery. *Remote Sensing*, 12(3), 422. https://doi.org/10.3390/rs12030422

NUR AND BACHMANN 19 of 21

om/doi/10.1029/2023JG007381 by UNIVERSITY OF VIRGINIA, Wiley Online Library on [14/11/2023]. See the Terms

- Ezenne, G., Jupp, L., Mantel, S., & Tanner, J. (2019). Current and potential capabilities of UAS for crop water productivity in precision agriculture. Agricultural Water Management, 218, 158–164. https://doi.org/10.1016/j.agwat.2019.03.034
- Gardner, C. M., Robinson, D., Blyth, K., & Cooper, J. D. (2000). Soil water content. In Soil and environmental analysis (pp. 13–76). CRC Press. Green, J. K., Seneviratne, S. I., Berg, A. M., Findell, K. L., Hagemann, S., Lawrence, D. M., & Gentine, P. (2019). Large influence of soil moisture on long-term terrestrial carbon uptake. Nature, 565(7740), 476–479. https://doi.org/10.1038/s41586-018-0848-x
- Hapke, B. (1981). Bidirectional reflectance spectroscopy: 1. Theory. Journal of Geophysical Research, 86(B4), 3039–3054. https://doi.org/10.1029/jb086ib04p03039
- Hapke, B. (1986). Bidirectional reflectance spectroscopy: 4. The extinction coefficient and the opposition effect. *Icarus*, 67(2), 264–280. https://doi.org/10.1016/0019-1035(86)90108-9
- Hapke, B. (2002). Bidirectional reflectance spectroscopy: 5. The coherent backscatter opposition effect and anisotropic scattering. *Icarus*, 157(2), 523–534. https://doi.org/10.1006/icar.2002.6853
- Hapke, B. (2008). Bidirectional reflectance spectroscopy: 6. Effects of porosity. Icarus, 195(2), 918–926. https://doi.org/10.1016/j.icarus.2008.01.003
- Hapke, B. (2012). Theory of reflectance and emittance spectroscopy. Cambridge university press.
- Harms, J. D., Bachmann, C. M., Ambeau, B. L., Faulring, J. W., Torres, A. J. R., Badura, G., & Myers, E. (2017). Fully automated laboratory and field-portable goniometer used for performing accurate and precise multiangular reflectance measurements. *Journal of Applied Remote Sensing*, 11(4), 046014. https://doi.org/10.1117/1.jrs.11.046014
- Hartman, B., & Domingue, D. (1998). Scattering of light by individual particles and the implications for models of planetary surfaces. *Icarus*, 131(2), 421–448. https://doi.org/10.1006/icar.1997.5861
- Helfenstein, P., & Shepard, M. K. (2011). Testing the Hapke photometric model: Improved inversion and the porosity correction. *Icarus*, 215(1), 83–100. https://doi.org/10.1016/j.icarus.2011.07.002
- Hunt, E. R., Daughtry, C. S., Mirsky, S. B., & Hively, W. D. (2014). Remote sensing with simulated unmanned aircraft imagery for precision agriculture applications. *Ieee Journal of Selected Topics in Applied Earth Observations and Remote Sensing*, 7(11), 4566–4571. https://doi. org/10.1109/jstars.2014.2317876
- Hyperspectral and operational software. (2023). Retrieved from https://www.headwallphotonics.com/products/software
- Jacquemoud, S., Baret, F., & Hanocq, J. (1992). Modeling spectral and bidirectional soil reflectance. Remote Sensing of Environment, 41(2–3), 123–132. https://doi.org/10.1016/0034-4257(92)90072-r
- Jaeger, E. B., & Seneviratne, S. I. (2011). Impact of soil moisture–atmosphere coupling on European climate extremes and trends in a regional climate model. Climate Dynamics, 36(9), 1919–1939. https://doi.org/10.1007/s00382-010-0780-8
- Kaputa, D. S., Bauch, T., Roberts, C., McKeown, D., Foote, M., & Salvaggio, C. (2019). MX-1: A new multi-modal remote sensing UAS payload with high accuracy GPS and IMU. In 2019 ieee systems and technologies for remote sensing applications through unmanned aerial systems (stratus) (pp. 1–4).
- Kirkby, M. (2016). Water in the critical zone: Soil, water and life from profile to planet. Soils, 2(4), 631-645. https://doi.org/10.5194/soil-2-631-2016
- Kisi, O., Shiri, J., & Tombul, M. (2013). Modeling rainfall-runoff process using soft computing techniques. Computers & Geosciences, 51, 108–117. https://doi.org/10.1016/j.cageo.2012.07.001
- L3harris ENVI. (2023). Retrieved from https://www.l3harrisgeospatial.com/Software-Technology/ENVI
- Lekner, J., & Dorf, M. C. (1988). Why some things are darker when wet. Applied Optics, 27(7), 1278–1280. https://doi.org/10.1364/ao.27.001278
 Li, W., Liu, C., Yang, Y., Awais, M., Ying, P., Ru, W., & Cheema, M. (2022). A UAV-aided prediction system of soil moisture content relying on thermal infrared remote sensing. International journal of Environmental Science and Technology, 19(10), 1–14. https://doi.org/10.1007/s13762-022-03958-7
- McCorkel, J., Bachmann, C. M., Coburn, C., Gerace, A. D., Leigh, L., Czapla-Myers, J. S., et al. (2017). Overview of the 2015 algodones sand dunes field campaign to support sensor intercalibration. *Journal of Applied Remote Sensing*, 12(1), 012003. https://doi.org/10.1117/1.ics.12.012003
- McLoughlin, S. M., Wiberg, P. L., Safak, I., & McGlathery, K. J. (2015). Rates and forcing of marsh edge erosion in a shallow coastal bay. Estuaries and Coasts. 38(2), 620–638. https://doi.org/10.1007/s12237-014-9841-2
- Mohanty, B. P., Cosh, M. H., Lakshmi, V., & Montzka, C. (2017). Soil moisture remote sensing: State-of-the-science. *Vadose Zone Journal*, 16(1), 1–9. https://doi.org/10.2136/vzj2016.10.0105
- Mulder, V., De Bruin, S., Schaepman, M. E., & Mayr, T. (2011). The use of remote sensing in soil and terrain mapping—A review. *Geoderma*, 162(1-2), 1-19. https://doi.org/10.1016/j.geoderma.2010.12.018
- NASA surface biology and geology mission science and applications traceability matrix. (2023). Retrieved from https://sbg.jpl.nasa.gov/satm/ SBG_SATM_Draft_v301.xlsx/view
- Nelder, J. A., & Mead, R. (1965). A simplex method for function minimization. The Computer Journal, 7(4), 308–313. https://doi.org/10.1093/comin/7.4.308
- Nicodemus, F. E., Richmond, J. C., & Hsia, J. J. (1977). Geometrical considerations and nomenclature for reflectance.
- Nur, N. B., & Bachmann, C. M. (2023). Associated Data and Code for 'Comparison of Soil Moisture Content Retrieval Models Utilizing Hyper-spectral Goniometer Data and Hyperspectral Imagery from an Unmanned Aerial System' (Version v.1.0.3) [Dataset and Computer Software]. Zenodo. https://doi.org/10.5281/ZENODO.8021935
- Ochsner, T. E., Cosh, M. H., Cuenca, R. H., Dorigo, W. A., Draper, C. S., Hagimoto, Y., et al. (2013). State of the art in large-scale soil moisture monitoring. Soil Science Society of America Journal, 77(6), 1888–1919. https://doi.org/10.2136/sssaj2013.03.0093
- Olofsson, P., & Andersson, M. (2012). Probability, statistics, and stochastic processes. John Wiley & Sons.
- Osgood, D. T., & Zieman, J. C. (1993). Spatial and temporal patterns of substrate physicochemical parameters in different-aged barrier island marshes. Estuarine. Coastal and Shelf Science, 37(4), 421–436. https://doi.org/10.1006/ecss.1993.1065
- Padró, J.-C., Carabassa, V., Balagué, J., Brotons, L., Alcañiz, J. M., & Pons, X. (2019). Monitoring opencast mine restorations using unmanned aerial system (UAS) imagery. Science of the Total Environment, 657, 1602–1614. https://doi.org/10.1016/j.scitotenv.2018.12.156
- Palace, M., Herrick, C., DelGreco, J., Finnell, D., Garnello, A. J., McCalley, C., et al. (2018). Determining subarctic peatland vegetation using an unmanned aerial system (UAS). Remote Sensing, 10(9), 1498. https://doi.org/10.3390/rs10091498
- Palmer, K. F., & Williams, D. (1974). Optical properties of water in the near infrared. JOSA, 64(8), 1107–1110. https://doi.org/10.1364/josa.64.001107
- Petropoulos, G. P., Srivastava, P. K., Piles, M., & Pearson, S. (2018). Earth observation-based operational estimation of soil moisture and evapotranspiration for agricultural crops in support of sustainable water management. Sustainability, 10(1), 181. https://doi.org/10.3390/su10010181

NUR AND BACHMANN 20 of 21

elibrary.wiley.com/doi/10.1029/2023JG007381 by UNIVERSITY OF VIRGINIA, Wiley Online Library on [14/11/2023]. See the Terms

- Rakha, T., & Gorodetsky, A. (2018). Review of unmanned aerial system (UAS) applications in the built environment: Towards automated building inspection procedures using drones. Automation in Construction, 93, 252–264. https://doi.org/10.1016/j.autcon.2018.05.002
- Robinson, D. A., Campbell, C. S., Hopmans, J. W., Hornbuckle, B. K., Jones, S. B., Knight, R., et al. (2008). Soil moisture measurement for ecological and hydrological watershed-scale observatories: A review. *Vadose Zone Journal*, 7(1), 358–389. https://doi.org/10.2136/ vzi2007.0143
- Rochester Institute of Technology. (2023). Research Computing Services. Rochester Institute of Technology. https://doi.org/10.34788/0S3G-QD15Roth, B. D., Saunders, M. G., Bachmann, C. M., & van Aardt, J. (2021). Leaf bidirectional transmittance distribution function estimates and models for select deciduous tree species. IEEE Transactions on Geoscience and Remote Sensing, 60, 1–14. https://doi.org/10.1109/tgrs.2021.3052877
- Roth, B. D., Saunders, M. G., Bachmann, C. M., & van Aardt, J. A. (2020). On leaf BRDF estimates and their fit to microfacet models. Ieee Journal of Selected Topics in Applied Earth Observations and Remote Sensing, 13, 1761–1771. https://doi.org/10.1109/jstars.2020.2988428
- Schaepman-Strub, G., Schaepman, M. E., Painter, T. H., Dangel, S., & Martonchik, J. V. (2006). Reflectance quantities in optical remote sensing-definitions and case studies. Remote Sensing of Environment, 103(27–42), 27–42. https://doi.org/10.1016/j.rse.2006.03.002
- Schmidt, F., & Fernando, J. (2015). Realistic uncertainties on Hapke model parameters from photometric measurement. *Icarus*, 260, 73–93. https://doi.org/10.1016/j.icarus.2015.07.002
- Shafian, S., Rajan, N., Schnell, R., Bagavathiannan, M., Valasek, J., Shi, Y., & Olsenholler, J. (2018). Unmanned aerial systems-based remote sensing for monitoring sorghum growth and development. PLoS One, 13(5), e0196605. https://doi.org/10.1371/journal.pone.0196605
- Shepard, M. K., & Helfenstein, P. (2007). A test of the Hapke photometric model. *Journal of Geophysical Research*, 112(E3), E03001. https://doi.org/10.1029/2005je002625
- Shepard, M. K., & Helfenstein, P. (2011). A laboratory study of the bidirectional reflectance from particulate samples. *Icarus*, 215(2), 526–533. https://doi.org/10.1016/j.icarus.2011.07.033
- Shepherd, A., McGinn, S., & Wyseure, G. (2002). Simulation of the effect of water shortage on the yields of winter wheat in north-east England. Ecological Modelling, 147(1), 41–52. https://doi.org/10.1016/s0304-3800(01)00405-7
- Shiltz, D. J., & Bachmann, C. M. (2023). An alternative to Hapke's macroscopic roughness correction. Icarus, 390, 115240. https://doi.org/10.1016/j.icarus.2022.115240
- Shukla, A., & Karki, H. (2016). Application of robotics in onshore oil and gas industry—A review part i. Robotics and Autonomous Systems, 75, 490–507. https://doi.org/10.1016/j.robot.2015.09.012
- Smith, R. S., Yeend, W., Dohrenwend, J., & Gese, D. (1984). Mineral resources of the north algodones dunes wilderness study area (CDCA-360), imperial county, California (Tech. Rep.). Geological Survey, Bureau of Mines.
- Stern, F. (1964). Transmission of isotropic radiation across an interface between two dielectrics. Applied Optics, 3(1), 111–113. https://doi.org/10.1364/ao.3.000111
- Stocker, B. D., Zscheischler, J., Keenan, T. F., Prentice, I. C., Seneviratne, S. I., & Peñuelas, J. (2019). Drought impacts on terrestrial primary production underestimated by satellite monitoring. *Nature Geoscience*, 12(4), 264–270. https://doi.org/10.1038/s41561-019-0318-6
- Storn, R., & Price, K. (1997). Differential evolution—a simple and efficient heuristic for global optimization over continuous spaces. *Journal of Global Optimization*. 11(4), 341–359. https://doi.org/10.1023/a:1008202821328
- Tyler, A. C., Mastronicola, T. A., & McGlathery, K. J. (2003). Nitrogen fixation and nitrogen limitation of primary production along a natural marsh chronosequence. *Oecologia*, 136(3), 431–438. https://doi.org/10.1007/s00442-003-1277-5
- Tyler, A. C., & Zieman, J. C. (1999). Patterns of development in the Creekbank region of a barrier island spartina alterniflora marsh. Marine Ecology Progress Series, 180, 161–177. https://doi.org/10.3354/meps180161
- Van Es, H., & Schindelbeck, R. (2003). Field procedures and data analysis for the Cornell sprinkle infiltrometer. Department of Crop and Soil Science Research. Series R03-01. Soil Health. Cals. Cornell. Edu.
- Vereecken, H., Huisman, J., Bogena, H., Vanderborght, J., Vrugt, J., & Hopmans, J. (2008). On the value of soil moisture measurements in vadose zone hydrology: A review. Water Resources Research, 44(4). https://doi.org/10.1029/2008wr006829
- Verhoef, W., & Bach, H. (2007). Coupled soil—leaf-canopy and atmosphere radiative transfer modeling to simulate hyperspectral multi-angular surface reflectance and toa radiance data. Remote Sensing of Environment, 109(2), 166–182. https://doi.org/10.1016/j.rse.2006.12.013
- Viewspec pro software. (2023). Retrieved from https://www.malvernpanalytical.com/en/support/product-support/software/viewspecprosoftwareinstall
- Virginia coast reserve long term ecological research site. (2023). Retrieved from https://www.vcrlter.virginia.edu/home2/
- Wang, L., & Qu, J. J. (2009). Satellite remote sensing applications for surface soil moisture monitoring: A review. Frontiers of Earth Science in China, 3(2), 237–247. https://doi.org/10.1007/s11707-009-0023-7
- Wu, Y., Gong, P., Liu, Q., & Chappell, A. (2009). Retrieving photometric properties of desert surfaces in China using the Hapke model and MISR data. Remote Sensing of Environment, 113(1), 213–223. https://doi.org/10.1016/j.rse.2008.09.006
- Yang, G.-J., Zhao, C.-J., Huang, W.-J., & Wang, J.-H. (2011). Extension of the Hapke bidirectional reflectance model to retrieve soil water content. Hydrology and Earth System Sciences, 15(7), 2317–2326. https://doi.org/10.5194/hess-15-2317-2011
- Yang, X., Yu, Y., & Li, M. (2019). Estimating soil moisture content using laboratory spectral data. *Journal of Forestry Research*, 30(3), 1073–1080. https://doi.org/10.1007/s11676-018-0633-6
- Young, D. R., Porter, J. H., Bachmann, C. M., Shao, G., Fusina, R. A., Bowles, J. H., et al. (2007). Cross-scale patterns in shrub thicket dynamics in the Virginia barrier complex. Ecosystems, 10(5), 854–863. https://doi.org/10.1007/s10021-007-9084-1
- Zhao, P., Zhou, Y., Li, F., Ling, X., Deng, N., Peng, S., & Man, J. (2020). The adaptability of APSIM-wheat model in the middle and lower reaches of the Yangtze River plain of China: A case study of winter wheat in Hubei province. *Agronomy*, 10(7), 981. https://doi.org/10.3390/agronomy10070981

Erratum

In the originally published article, the brackets encompassing lambda were missing in equation 21 and the subsequent line of text. The brackets have now been added correcting the model's mathematical meaning and structure. This may be considered the authoritative version of record.

NUR AND BACHMANN 21 of 21